

WIRE: Watershed based iris recognition

Maria Frucci^a, Michele Nappi^b, Daniel Riccio^{c,*}, Gabriella Sanniti di Baja^{a,d}

^a Istituto Calcolo e Reti ad Alte Prestazioni, CNR, Via P. Castellino 111, I-80131 Napoli, Italy

^b Università di Salerno, via Giovanni Paolo II, Fisciano I-84084, Italy

^c Università di Napoli Federico II, via Cintia, I-80126 Napoli, Italy

^d Istituto di Cibernetica E. Caianiello, CNR, Via Campi Flegrei 34, I-80078 Pozzuoli (Napoli), Italy

ABSTRACT

A Watershed transform based Iris REcognition system (WIRE) for noisy images acquired in visible wavelength is presented. Key points of the system are: the color/illumination correction pre-processing step, which is crucial for darkly pigmented irises whose albedo would be dominated by corneal specular reflections; the criteria used for the binarization of the watershed transform, leading to a preliminary segmentation which is refined by taking into account the watershed regions at least partially included in the best iris fitting circle; the introduction of a new cost function to score the circles detected as potentially delimiting limbus and pupil. The advantage offered by the high precision of WIRE in iris segmentation has a positive impact as regards the iris code, which results to be more accurately computed, so that the performance of iris recognition is also improved. To assess the performance of WIRE and to compare it with the performance of other available methods, two well known databases have been used, specifically UBIRIS version 1 session 2 and the subset of UBIRIS version 2 that has been used as training set for the international challenge NICE II.

1. Introduction

Iris recognition is one of the more commonly used biometrics. It is generally regarded as the most accurate of the commonly used biometric technologies, giving a reliable answer to the increasing demand of security systems [1]. This is due to the good features characterizing the iris of human beings (richness, uniqueness, external visibility and stability during the entire life) and to the non-invasiveness of the available iris acquisition technologies (cameras operating in the near infrared spectrum [2,3] or with visible light technology [4], able to capture good quality images at a largely variable distance (from a few centimeters up to a few meters) and even “on-the-move” [5–7]).

The literature in the field of iris detection and recognition has received a considerable number of contributions, since the first system has been suggested by Daugman [8]. A recent book, [9], providing complete coverage of the key subjects in iris recognition – from sensor acquisition to matching – and two wide surveys of iris recognition methods covering the periods until the end of 2007, [10], and from 2008 to 2010, [11], are available.

The iris is the annular part of the eye delimited by the white sclera and delimiting the pupil, which even in case of eye colors having the lightest tints of blue is the darkest part of the eye (see Fig. 2). The structure of the iris is referred to as the iris texture and has a number of characteristics significantly larger than the number of characteristics typical of other biometrics. Though an interesting debate has recently started on the stability of the iris pattern [12–14], the literature has widely shown that the probability of obtaining similar signatures from two different iris textures is close to zero [1]. Thus, at least under nearly ideal image acquisition conditions (good illumination and cooperative subject), simple image processing tools can be satisfactorily adopted for iris recognition. In turn, under non-ideal conditions, problems such as occlusions caused by eyelids and eyelashes, poor illumination, specular reflection and lack of cooperation of the subject whose identity should be detected, make iris recognition a hard task to face.

The main weakness of iris recognition techniques developed in the last years is that they show a proven effectiveness only in relatively constrained scenarios, performing in the near infrared spectrum and at close acquisition distances. So recently, several researchers have focused their attention on designing a novel family of iris segmentation algorithms operating on images acquired in less constrained conditions and under the visible light. However, the unconstrained iris image acquisition introduces additional noise factors as reflections, blurring and defocus, mainly

* Corresponding author.

E-mail addresses: maria.frucci@cnr.it (M. Frucci), mnappi@unisa.it (M. Nappi), daniel.riccio@unina.it (D. Riccio), gabriella.sannitidibaja@cnr.it (G. Sanniti di Baja).

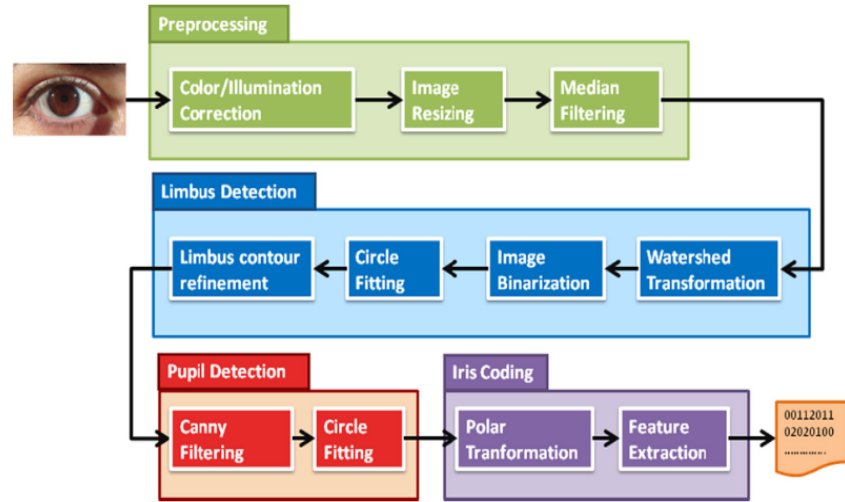


Fig. 1. Flow chart of WIRE.



Fig. 2. Images of two subjects from the UBIRIS2t dataset, acquired in uncontrolled environment under different illumination conditions before (left and middle left) and after (middle right and right) the color/illumination correction. (For interpretation of the references to color in this figure, the reader is referred to the web version of this article.)

due to subjects moving at widely varying distances. To solve the problem of the detection and recognition of heavily degraded iris images, the scientific community promoted two international evaluation initiatives about these issues, named Noisy Iris Challenge Evaluation (NICE) [7]. This competition was divided in two parts: (i) Part I – for the segmentation of iris images in visible wavelength and (ii) Part II– for the recognition of iris images in visible light.

Iris recognition includes a number of processes: (i) acquisition of the eye image, (ii) iris segmentation, to separate the foreground (iris and pupil) from the background (the rest of the image), (iii) normalization, to produce iris regions with the same constant dimensions, so that images of the same iris taken under different conditions have their features at the same spatial locations, (iv) features extraction, to associate a code to each detected iris, and (v) recognition, generally accomplished by using mathematical and statistical algorithms to compare the code of the iris at hand with the codes stored in a suitable database. All processes (i)–(v) should be accomplished in accurate way, since the result at each step conditions the outcome of the successive step.

Though this paper introduces the iris recognition system WIRE and, hence, deals with all the above processes, in what follows we will focus mainly on the novel contribution of this paper, i.e., on iris segmentation for degraded iris images acquired in visible wavelength. Iris segmentation is obtained by using both watershed transformation and circle fitting. In this way, we identify the iris boundary more precisely than by resorting only to circle fitting, and obtain an accurately computed iris code. Using the watershed transform is important since the shape of the iris is not necessarily circular and because pixels inside the best fitting circle may be noisy iris pixels. To assess the performance of WIRE, we adopt two well known databases: UBIRIS version 1 session 2 (UBIRISv1s2) [15] and the subset of UBIRIS version 2 that has been used as training set in NICE (UBIRISv2t) [16].

The rest of the paper is organized as follows. Previous work for iris segmentation is briefly reviewed in Section 2. The segmentation scheme of the proposed system WIRE for watershed based iris recognition is described in Section 3. Section 4 deals with iris recognition. Section 5 discusses parameter setting. Section 6 is devoted to the experiments and to the discussion of the obtained results. Concluding remarks and some ideas for future work are finally given in Section 7.

2. Related works on iris segmentation

The role of iris segmentation is to identify in the image of the eye all pixels belonging to the iris. Note that pixels in positions where iris pixels are expected may be noisy pixels and should not contribute to the computation of the iris code. Segmentation is a crucial task since inaccuracy in iris detection has a strong negative impact on the performance of the whole recognition task.

Iris segmentation is generally achieved by identifying the boundary of the pupil and of the limbus, so as to delimit the region of interest in the image, and by suitably taking into account that eyelids and eyelashes may overlap with the iris causing interruptions of its boundary.

Methods for iris segmentation can be roughly divided into two categories: (i) methods approximating the iris boundary with a circle or an ellipse, and (ii) methods determining the precise boundary of the iris. Methods in the former category are often referred to as classical methods.

A well known classical method employs the integro-differential operator [3]. The input image is preliminarily convolved with a Gaussian filter to obtain a smoothed image. In this way, noise is reduced without affecting the strongest edges, i.e., those in correspondence with the boundaries of iris and eyelids. Then, by means of an integro-differential operator, the maximum value of a

normalized integral is detected along circular contours characterized by different radii and positions of the center. The integro-differential operator acts as an iterative circular edge detector, which identifies the boundary of pupil and iris. Since eyelids may partially occlude the iris, the limbus boundary may be not circular. To detect the boundary of the eyelids and, hence, correctly identify the iris, the integration arc used is suitably changed from circular to arcuate.

Another classical method is due to Wildes [2]. This is a histogram-based model-fitting approach involving the use of the Hough Transform [17]. After an edge map of the eye image is obtained by means of a gradient operator, a voting procedure is used to select the parameter values for the contour that better fits a circle. Also in this case, the eye image is preliminarily smoothed. Derivatives corresponding to vertical edges of the limbus boundary are weighted more during the voting process. In this way, even if the eyelids partially overlap the iris, a circle can be detected fitting the lateral parts of the limbus boundary. Notwithstanding its quite high computational cost, the Hough transform is still often used [18]. To find the boundaries of upper and lower eyelids, a gradient operator favoring horizontal edges is used and the parameter values of contours that better fit parabolic arcs are computed. An alternative way to detect the best fitting circle has been suggested in ISIS [19], which is based on Taubin's technique [20]. Other recent iris segmentation methods approximating the iris boundaries with circles, ellipses or polynomials are available in [21–24].

Geodesic active contours [25,26], and variational level sets [27,28], are used in methods aimed at determining the precise iris boundary, particularly in the presence of occlusions caused by eyelashes. The relation between active contours and minimal length curves is considered for methods based on geodesic active contours. A curve, initialized arbitrarily within the iris, evolves by taking into account properties of the iris boundary, until it satisfies a stopping criterion. The difference in energy between successive contours is taken into account to avoid over-evolution, occurring in regions where the stopping criterion is not sufficiently strong. In turn, the approach based on variational level sets uses partial differential equations to find a numerical solution for the curves defining the iris boundaries. The iris boundaries are first approximated using elliptical models. Then, they are refined using active contours with variational formulation. The method identifies the curve within the level set function that minimizes the total energy of the curve. Other recent methods based on curve evolution to precisely detect the iris boundaries can be found in [29,30].

Though the watershed transformation, introduced in [31] to partition gray level images, is generally recognized as an image segmentation tool able to correctly detect objects contours, to our knowledge it has not been much used in the framework of iris segmentation [32–34]. In this paper we will extensively make use of the watershed transformation.

Our iris segmentation method borrows from the classical methods the idea of using circle fitting. However, we use circle fitting only to identify the Region Of Interest (ROI), where to detect more accurately the iris boundary. Moreover, circle fitting is done on a binarized version of the watershed transform of the eye image, obtained by taking into account local and global properties in the eye image. Once the ROI has been identified by circle fitting, the watershed transform is furthermore exploited to distinguish, among all the watershed regions at least partially overlapping the best fitting circle, those actually belonging to the iris from those belonging to the eyelids, eyelashes, sclera, or to reflection regions. In this respect, differently from other techniques (e.g., [35]) that explicitly face problems such as those due to reflections and eyelashes, the watershed transform provides without any further cost the additional advantage to distinguish regions that, though placed within

the iris, should not be taken into account when computing the iris code since they would provide a noisy contribution.

Our iris segmentation method is the improved version of recently suggested methods [33,34] and shows the following main differences: (i) the introduction of a color/illumination correction step, (ii) a completely revised process to select the best fitting circle for the limbus, (iii) a new method to improve the location of the pupil, once the iris region has been isolated from the input image, and (iv) an extensive evaluation of the impact induced on recognition by the better segmentation and its comparison with that of other methods (to this purpose, we use using an improved version of an algorithm taken from the state of the art [36]). More in general, the main novelties of WIRE are the new curvature approximation method, the cost function used to score circles approximating the boundary, and the use of the watershed transformation to obtain a more precise iris boundary.

3. Segmentation framework

WIRE works with RGB color images, where pixel colors are interpreted as points in the 3D Cartesian space with red (R), green (G) and blue (B) as coordinate axes. Since the R, G, B coordinates of any pixel color are in the range [0,255], all possible colors are points within a cube spanning from the origin (0, 0, 0), black, to (255, 255, 255), white.

Iris segmentation consists of six phases respectively devoted to pre-processing, watershed transformation, image binarization, circle fitting, limbus contour refinement, and pupil detection. See the flow-chart in Fig. 1.

3.1. Pre-processing

Pre-processing includes color/illumination correction, size reduction, image smoothing, and gradient image computation.

The goal of color/illumination correction is to reduce local distortions, as shadows and different color temperature, introduced during uncontrolled iris acquisition, as well as to treat both dark brown eyes and light blue eyes.

On the basis of the Lambertian reflectance theory [37], the image intensity of the diffusely reflected light I is as follows:

$$I(x, y) = R_f(x, y)L(x, y) \quad (1)$$

where R_f is the albedo, or reflectance component, and L is the intensity of the incoming light. Consequently, the R_f component can be computed as the ratio, pixel by pixel, between the image I and the version of I smoothed by a Gaussian filter.

Based on the above concepts, to build a smoothed version of the eye image, WIRE applies a Gaussian filter to each of the three RGB components using experimentally fixed values for kernel dimension n and variance σ (for the assignment of values to n and variance σ see Section 5). An array with the same resolution of the examined color component is computed, where at each position the ratio pixel by pixel between the color component and its filtered version is recorded. These values are then normalized, [38], in the range [0,1] by means of a Quasi Linear Sigmoidal function and are then mapped in the range [0,255], generating the new image component. In Fig. 2, two color input images and the corresponding results after color/illumination correction are shown. It can be seen that a clearer separation of the eye parts is available after color/illumination correction. The two eye images are taken from the UBIRISv2t database. Their size is 400×300 , as it is for all other images in the database. The eye in Fig. 2 left is used as running example.

Size reduction and smoothing are respectively accomplished to reduce the computation time necessary for the successive phases of the process and to reduce the noise in the eye images.

In order to speed up the computation without biasing the quality of the input image, a resizing to 200×150 pixels is performed by means of standard scaling down based on linear interpolation and using a reduction factor of 0.5. Then, a median filter is applied to the image I . By taking into account that the iris diameter is comparable to the vertical resolution of the filter, size has been set to 7×7 . As a result, noise is removed while edges are preserved. See Fig. 3 left, showing the resized and smoothed image. For better visualization all images appear from now on with the same size as the input images.

Finally, computing the gradient image is done to enhance the edges present in the eye images and to identify the regional minima necessary for the watershed transformation.

The Sobel edge filter is applied to each of the three gray level images R , G and B composing I . The gradient image ∇I , Fig. 3 middle left, is obtained as the average of the three computed gradient images.

3.2. Watershed transformation

The watershed transformation partitions a gray level image by applying region growing to a suitable set of seeds. Seeds are generally detected as the regional minima in the gradient image and region growing is accomplished by taking into account some homogeneity criterion, so that each region of the partition will result to be homogeneous, while the union of any two adjacent regions will not.

Two main approaches can be followed to compute the watershed transform, known as watershed transform by immersion and watershed transform by topographical distance [39]. In this paper, we follow the latter approach. The watershed lines of the watershed transform W are shown to be superimposed on a white background for better visibility in Fig. 3 middle right. Of course the watershed lines can also be seen as separating lines of the regions into which the eye image I is partitioned.

With reference to Fig. 3 middle right, we observe that watershed lines satisfactorily border the regions into which the eye image is partitioned, but their number is rather large so making segmentation a very complex task. To simplify the segmentation process, we perform merging of adjacent regions that are similar

to each other as far as their color is concerned. To this purpose, the average color of any region R_i of the watershed transform is computed as the mean value of the colors of pixels belonging to it and the Euclidean distance in color between R_i and each of its adjacent regions is computed. Then, R_i is merged with the adjacent region R_j at the minimum color distance from R_i , provided that the distance between R_i and R_j is lower than an a priori fixed threshold δ (see Section 5). The watershed lines resulting after merging are shown in Fig. 3 right.

To perform segmentation, we should identify the regions belonging to the iris among all the obtained watershed regions.

Regions of the watershed partitioned image I consist of pixels characterized by a homogeneous color. Thus, we can work on a modified version Q of I , where the colors of pixels in the same region R_i are replaced by a unique representative color. The representative color for a region R_i is the color c_i whose red, green and blue components are the arithmetic means of the red, green and blue components of the colors of all pixels in R_i . The resulting image Q can be seen in Fig. 4 left.

3.3. Image binarization

To detect the ROI where the limbus boundary is placed, we compute a binarized version BW of the watershed transform. Binarization is done in such a way that even if the foreground of BW does not coincide exactly with the region of the eye consisting of iris and pupil, its contour includes portions of the limbus boundary that are large enough to reliably apply circle fitting.

For each region R_i , we respectively denote by db_i and dw_i the Euclidean distances of its representative color c_i from black and white in the RGB space. Moreover, we denote by db and dw the arithmetic means of the distances of all representative colors from black and white. Finally, we denote by dbw the distance between black and white. Since black and white are the two points in the 3D cube having respectively coordinates $(0, 0, 0)$ and $(255, 255, 255)$, it results $dbw = 441.6730$.

BW is obtained by ascribing the foreground status to the partition regions that can be tentatively regarded as belonging to iris or pupil, and the background status to all other partition regions. Binarization is accomplished in two steps.

In general pupil and iris are characterized by colors that are closer to black than to white, while sclera and eyelids have color closer to white than to black. Thus, during the first step of

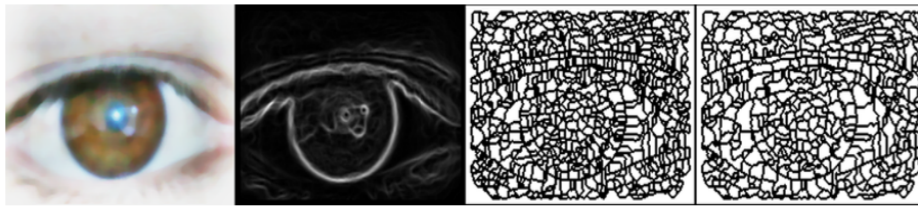


Fig. 3. Effect of resizing and median filter, left, gradient image, middle left, watershed transform, middle right, and watershed transform after merging, right.



Fig. 4. The image Q obtained by replacing the colors within each region of W by the representative color of the region, left. The binary image BW , after the first step of binarization of the watershed transform, middle, and after the second step, right.

binarization, the two arithmetic means db and dw could be used as threshold values on the representative colors to decide on the status of the corresponding partition regions. If for c_i it results in $db_i \leq db$, the status of foreground could be ascribed to R_i . In turn, if $dw_i \leq dw$, the status of background could be ascribed to R_i . Obviously, if it is $db_i > db$ and $dw_i > dw$, a decision on the status of R_i could not be taken. Moreover, if it is $db_i \leq db$ and $dw_i \leq dw$ both the foreground status and the background status might be ascribed to R_i . Thus, the status might be not ascribed to all regions, or the status might be ascribed in an ambiguous manner. The former case happens if it results in $db+dw < dbw$, while the latter case when it results in $db+dw \geq dbw$.

The above problems can be overcome by fixing a non ambiguous and proper value for the binarization threshold T . To this aim, the ratio $dbw/(db+dw)$ is used as a multiplicative weight for the arithmetic mean db , and T is set to $db \times dbw/(db+dw)$. The binary image BW is obtained by ascribing the foreground status to the regions whose representative colors have distance from black smaller than T , and the background status to all other regions. The result of the first step of binarization is shown in Fig. 4 middle.

During the second step of binarization, BW is refined by changing from foreground to background the status of some regions. To this aim, let c_F and c_B denote the average foreground color and average background color, respectively. These average colors are computed as the arithmetic means of the colors of the pixels belonging to regions of Q that have been tentatively assigned to the foreground and to the background. The refined image BW is obtained by changing the status from foreground to background of any region R_i , such that $d(c_i, c_B) \leq d(c_i, c_F)$, where d is the Euclidean. The binary image resulting after the second step of binarization is shown in Fig. 4 right.

We remark that the utility of the watershed transform is related to the high quality of the found boundaries. In fact, the watershed lines along the contour of the foreground include pixels that in the gradient image ∇I are located in correspondence with strong changes in color of the eye image. Thus, the edges of the foreground of BW are placed in correspondence of the perceived boundaries.

3.4. Circle fitting

The circle detection procedure [20] is applied to the contour of the foreground of BW , which includes both very smooth portions (shown in yellow in Fig. 5 left), and sharp bends (shown in blue in Fig. 5 left). The existence of sharp bends facilitates segmentation of the contour into subsets that can then undergo circle fitting. To avoid a time consuming point by point curvature analysis, we resort to an estimate of curvature, by adopting the following strategy:

- Each connected component C of the contour is processed by a countour tracing algorithm to orderly record its points $P_k=(x_k, y_k)$ in a list $L_C=\{P_1, P_2, \dots, P_n\}$.
- Starting from a point P_k and moving along the contour L_C , the additional contour point taken into account is the point P_{k+t} at

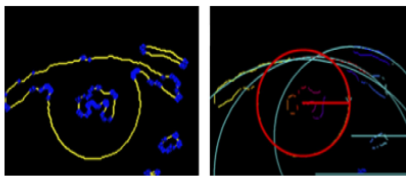


Fig. 5. The contour of the binarized version BW of the watershed transform, left, and circles detected by the Taubin algorithm (the best ranked circle is in red), right. (For interpretation of the references to color in this figure legend, the reader is referred to the web version of this article.)

distance t from P_k . Instead of taking the additional point P_{k+t} at a fixed distance from P_k , we set $t=4 \cdot \lfloor \log_2(|C|) \rfloor$ so as to take into account the length of the contour.

- Let $M=(m_x, m_y)$ be the midpoint of the segment $P_k P_{k+t}$ and let P_i be a contour point where $i=\lfloor (k+t)/2 \rfloor$. The Euclidean distance $d_{k,t}(M, P_i)$ is computed and is normalized by dividing it by the greatest of all distances $d_{\max} = \arg \max_k d_{k,t}$. Normalized distances are in the range $[0,1]$. The greater the distance value at a given point P_k is, the higher will be the corresponding estimated curvature.
- All points of C with a curvature larger than a threshold th_{curv} (see Section 5) are deleted from L_C , so that C is partitioned into a set of connected components of edges E_1, E_2, \dots, E_q with smooth curvature, as illustrated in Fig. 5 left.
- A new list of edges L_E is generated that is composed by the E_i including at least th_{pnt} contour points P_k (see Section 5). Taubin's algorithm [20] is then applied only to each E_i in L_E to provide both center and radius of circle approximation of iris (Fig. 5 right).

Among circles detected by Taubin's algorithm, some might not be entirely included into the image. Circles that are included for less than 80% are not further considered in the process, while the remaining ones undergo a voting procedure to select the best limbus approximation.

Let cf_i be the circle fitting E_i , and let (cf_{ix}, cf_{iy}) and r_i be its center and radius. Let us consider two additional circles cf'_i with radius $0.9r_i$ included in cf_i and cf''_i with radius $1.1r_i$ including cf_i . For each contour point in cf_i , in the polar coordinate system (ρ, θ) , WIRE computes the difference $diff_i$ between the two pixels of BW , which are located at the same angle θ , but with different radii in cf'_i and cf''_i . The differences $diff_i$ are summed up and the result is divided by the number of points in cf_i ; the obtained value is then assigned to the circle cf_i as its score. The circle cf_i with the maximum score is selected to approximate the limbus boundary (see the red circle in Fig. 5 right). The analysis of the limbus shows that outside red circle area falls mainly in the background, while the inner one in the foreground.

3.5. Limbus contour refinement

To identify as much correctly as possible the pixels actually belonging to iris and pupil, we exploit the information included in the watershed transform, in particular as regards the regions at least partially overlapping the circle found by circle fitting. In fact, the area identified by circle fitting may not include all pixels of the iris, and in turn may include also pixels belonging to eyelids, sclera and eyelashes, or iris pixels that are noisy pixels due to corneal specular reflections. Thus, the regions of W at least partially overlapping the found circle have to be analyzed individually. In Fig. 6 left, the detected circle is shown in purple superimposed on W . In Fig. 6 right, regions of W totally overlapping the circle are shown in red (if they are regions belonging to the foreground of

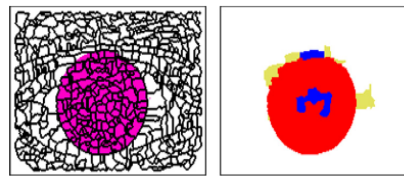


Fig. 6. Circle detected by circle fitting superimposed on W , left, regions of W totally overlapping the circle (red and blue) and regions partially overlapping the circle (yellow), right. (For interpretation of the references to color in this figure legend, the reader is referred to the web version of this article.)

BW) and blue (if they are regions belonging to the background of BW), while regions partially overlapping are shown in yellow.

Let c_{limbus} be the arithmetic mean of the colors of the pixels of Q that satisfy the following two conditions: (i) they are within the circle and (ii) they are in the foreground of BW. With reference to Fig. 4 right and Fig. 6 right, only the red regions and part of the yellow regions are taken into account to compute c_{limbus} . Analogously, let c_{back} be the arithmetic mean of the colors of the pixels of Q that are outside the circle and that have been assigned to the background in BW. Thus, with reference to Fig. 6, right, the blue regions are not taken into account in the computation of c_{back} .

Let us denote by f and b two markers that will be assigned to the watershed partition regions to indicate that a region is assigned to the foreground or to the background of the segmented image, respectively.

Watershed regions having no overlap at all with the circle are assigned the marker b . These regions belong by all means to the background. In turn, the remaining watershed regions are tentatively assigned to the foreground, but some further checking is necessary before taking a final decision. Thus, two foreground markers, f_+ and f_- , are initially introduced to distinguish watershed regions completely overlapping the circle (receiving the marker f_+) and watershed regions only partially overlapping the circle (receiving the marker f_-). In Fig. 6 right, red and blue regions are marked f_+ , while yellow regions are marked f_- .

Watershed regions with marker f_+ are analyzed first to validate some of them as foreground regions. This process is accomplished in two phases. During the first phase, the marker f_+ of any region R_i is changed into f if at least one of the following conditions is satisfied:

- 1) $d(c_i, c_{back}) > d(c_i, c_{limbus})$, where d is the Euclidean distance and c_i is the representative color c_i of R_i ; and
- 2) the region R_i has been assigned to the foreground in BW and at least a neighboring region of R_i has marker f_+ , while no neighboring regions exist with marker f_- .

During the second phase of the process, we compute the minimum Euclidean distance d_{min} between the representative color c_i of R_i and the representative color of each of the regions adjacent to R_i with marker f . Then, the marker of R_i is changed from f_+ to f , if $d(c_i, c_{back}) \geq d_{min}$. Otherwise, the marker of R_i is set to b .

Fig. 7 left, shows the regions with initial marker f_+ that have been detected as foreground regions (black) and as background regions (white), respectively.

Regions with marker f_- are then analyzed. Each watershed region with marker f_- is split in two sub-regions, which respectively include the pixels that are within the circle, and the pixels that are outside the circle. The former sub-regions play the role of regions completely overlapping the circle, and receive marker f_+ (red regions in Fig. 7 middle left). In turn, the latter sub-regions

play the role of regions that are not overlapping the circle, and receive marker b (green regions in Fig. 7 middle right).

After watershed region splitting, the image Q and the values c_{limbus} and c_{back} are updated since the number of regions and the relative representative colors have been modified. Then, final decision is taken for the regions with marker f_+ . Namely, each region R_i with marker f_+ is assigned to the foreground if there exists at least a neighboring region of R_i , already classified as belonging to the foreground, and at least one of the following cases occurs:

- i) $d(c_i, c_{back}) > d(c_i, c_{limbus})$;
- ii) the Euclidean distance between c_i and c_{back} is not smaller than the minimum Euclidean distance between c_i and the color of the regions adjacent to R_i and with marker f .

Otherwise, the region R_i with marker f_+ is assigned to the background.

The detected foreground is shown in Fig. 7 middle right. The representative colors of the foreground regions can be seen in Fig. 7 right.

In Fig. 8, the boundary of the foreground detected by WIRE is shown in red superimposed on a few sample eye images.

We point out that the detected foreground boundary may be multiply connected. In fact, besides the component identifying the limbus also other components are detected that delimit the light areas inside iris and pupil, which are mainly due to illumination. In this way, a more reliable coding of the iris is possible.

Moreover, we observe that the color/illumination correction has a key role in obtaining a more precise limbus. This can be appreciated with reference to Fig. 9, where the boundary detected for the eye images in Fig. 2 is shown. A better boundary identification is evident for the two images after color/illumination correction.

3.6. Pupil detection

To complete iris detection, the pupil boundary has to be identified. As the pupil is always inside the iris, the procedure for its detection is performed by considering only the portion of the whole eye image that is inside the circle approximating the limbus.

To this aim, the region of interest (ROI) is extracted from the input image after the color/illumination correction. The color ROI image is converted to a gray level image and is processed by the Canny filter in order to obtain 1-pixel thick contours. We used ten different thresholds and knowing that for the Canny filter threshold ranges from 0 to 1 the values we considered are {0.05, 0.10, 0.15, ..., 0.55}. For each image generated by Canny filter the corresponding connected components are extracted and pixel counting is performed. Only connected components including more than th_{pupil} pixels (see Section 5) are processed by Taubin circle fitting algorithm. A list of circles derived starting from connected components and entirely included in the circle

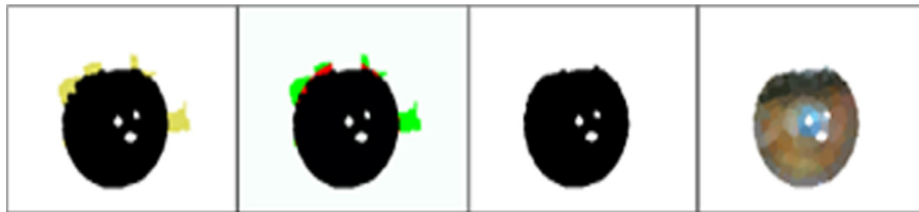


Fig. 7. Result after analyzing regions with marker f_+ , left; regions with initial marker f_- after splitting into sub-regions completely included by the circle (red) and outside the circle (green), middle left; area surrounded by the limbus, middle right; color quantized area surrounded by the limbus, right. (For interpretation of the references to color in this figure legend, the reader is referred to the web version of this article.)



Fig. 8. Some examples of detected foreground boundary. (For interpretation of the references to color in this figure, the reader is referred to the web version of this article.)

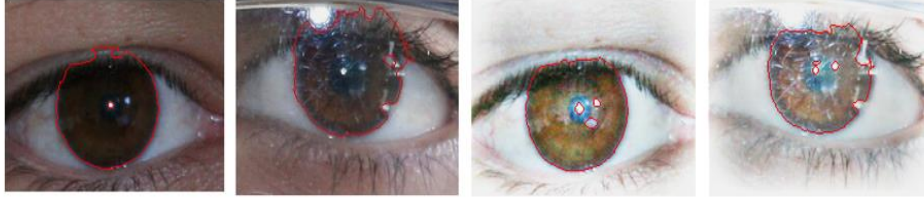


Fig. 9. Limbus, shown in red, detected without applying the color/illumination correction, left and middle left, and after applying the correction, middle right and right. (For interpretation of the references to color in this figure legend, the reader is referred to the web version of this article.)

approximating the limbus is generated. Each circle in the list is then processed by a voting function using the following criteria:

Homogeneity: The pupil is a circular region with a homogeneous gray level distribution. The voting function ignores if the pupil has bright or dark tones, because during uncontrolled acquisition this area is often affected by reflexes that could alter its appearance. Then, every circle receives a score calculated only according to the degree of homogeneity of the pixels it includes. If h is the histogram of the region included by the circle, the scoring function assigns to the circle a value s_h equal to

$$s_h = \max_i [h(i)] / \sum_{i=0}^{255} h(i). \quad (2)$$

Separability: The pupil boundary also shows a sharp transition from a darker to a lighter zone; thus a separability index is defined accordingly. Given a candidate circle C with its contour points represented in polar space as $P(\rho, \theta)$, WIRE considers the internal circle C_{IN} with $\rho_1 = 0.9\rho$, and the external circle C_{OUT} with $\rho_2 = 1.1\rho$. We define an operator, namely the separability, which is similar to Daugman's integro-differential operator that measures difference between the gray levels of corresponding pixels on such two concentric circles for each angle θ_i :

$$w(i) = |I(\rho_2 \cos(\theta_i), \rho_2 \sin(\theta_i)) - I(\rho_1 \cos(\theta_i), \rho_1 \sin(\theta_i))| \quad (3)$$

where $\theta_i = i\pi/180$ and $i = 1, 2, \dots, 360$. The pupil boundary separates the pupil from the iris, which significantly differs in color. Thus, $w(i)$ assumes values that are generally high and almost constant along all the pupil boundary, being characterized by a high mean and a low variance. Therefore, we can define the separability index as follows:

$$s_l = \frac{\bar{w}}{\sigma(w) + 1} \quad (4)$$

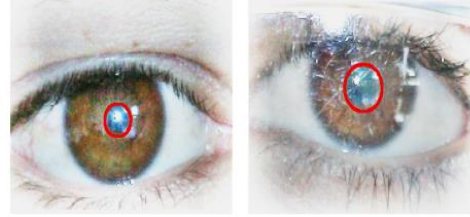


Fig. 10. The detected pupil boundary. (For interpretation of the references to color in this figure, the reader is referred to the web version of this article.)

The global score assigned to the circle C is

$$S = S_h + S_l. \quad (5)$$

The circle C_{max} with the highest score is considered as the circular shape which better approximates the pupil.

The pupil boundary found for the eye images in Fig. 2 middle right and right are shown in red in Fig. 10.

4. Iris recognition

The iris recognition process starts by isolating from the whole eye image (Fig. 11a) the iris. By using the process described in Section 3 for the detection of the boundaries of limbus and pupil, a binary image (Fig. 11b) is achieved that plays the role of binary mask, allowing iris isolation (Fig. 11c). Centre and radius of both iris and pupil are used to map the original annular iris region in the Cartesian space to a rectangular region (shown in Fig. 11d) in the polar space by means of the rubber sheet model. This approach was first introduced by Daugman in [3] to compensate for distortions caused by contraction/relaxation of muscles surrounding the pupil. Indeed, it is well known that is very unlikely for

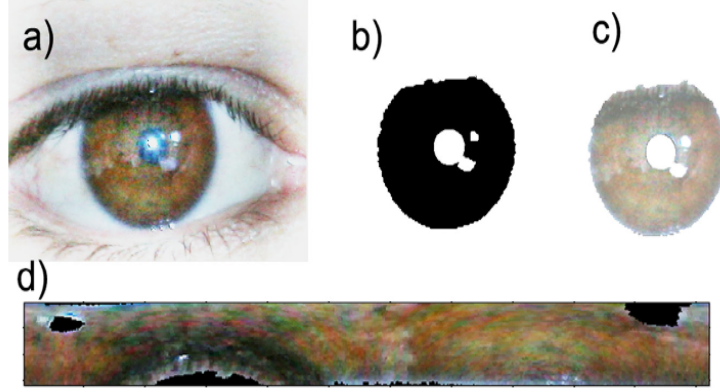


Fig. 11. Isolation and polar transformation of the iris annular region: (a) iris images after color and illumination correction, (b) binary mask with iris pixels in black, (c) iris annular region, and (d) iris pixels remapped in the polar space.

pupil to be perfectly concentric with respect to the iris. The polar iris image then undergoes a feature extraction technique to be represented in a low dimensional feature space. In particular, most of the approaches mentioned in Section 1 work on NIR or gray level images by extracting local features, which are very robust with respect to local distortions like partial occlusions caused by eyelids or eyelashes. In this specific context, color provides additional information that WIRE can exploit for both segmentation and classification. In general, it is possible to extend any of the gray level based approaches to the case of color images, by simply applying the technique separately to three R, G, B, channels and then gathering together individual results to obtain a global feature vector. WIRE performs in a completely different way, by keeping well disjoint features coming from color and luminance. This is achieved by mapping the original RGB image into the Hue, Saturation, Value (HSV) color space, so that H and S channels are processed together, while V is treated separately; an histogram based approach is adopted for Hue and Saturation, while cumulative sums method (CSUM) [36] is used for Value. CSUM has been adopted since it provides a good compromise between simplicity and effectiveness of the method.

In more details, an histogram h_H of 32 equidistributed bins is computed over the H channel, whose elements are normalized into the range $[0,1]$ by dividing them by the total number of pixels in the eye image. Similarly, the histogram h_S is extracted from the S channel. The color feature vector is represented by a global histogram h_{HS} of 64 bins, which is obtained by concatenating h_H and h_S . The distance between two color feature vectors is computed by the cosine dissimilarity and is mapped into the range $[0,1]$ (the original range is $[-1,1]$).

Luminance, that is the V channel, is processed through the CSUM approach to extract local features. CSUM has been shown to be very robust with respect to the noise affecting UBIRIS version 1 and 2 iris images and provided a recognition accuracy that is comparable with the state of the art.

CSUM partitions the input iris image into a number of cells, where each cell A_k has size $u \times v$ (see Section 5 for the assignment of u and v). For each A_k , CSUM computes the average gray value $avg(A_k)$ of its pixels. Along orthogonal directions (horizontal and vertical), cells A_k are aggregated into sets $\Omega_i = \{A_1, A_2, \dots, A_q\}$ of q cells and the average gray value is calculated for each set as follows:

$$avg(\Omega_i) = \frac{1}{q} \sum_{k=1}^q avg(A_k) \quad (6)$$

Given a cell A_k , its cumulative sum S_k is computed as

$$S_k = S_{k-1} + [avg(A_k) - avg(\Omega_i)] \quad (7)$$

where $S_0=0$ and $k=1,2,\dots,q$. The iris code is then computed by applying the following rules:

Let S_{max} and S_{min} be the maximum and minimum values respectively that S_k can assume in the sets Ω_i , then:

- If S_k falls between S_{max} and S_{min} :
 - if $S_k \geq S_{k-1}$, assign Ω_i with 1;
 - if $S_k < S_{k-1}$, assign Ω_i with 2;
- else assign Ω_i with 0.

The dissimilarity between two iris codes is computed as their Hamming distance normalized in the range $[0,1]$. Finally, the overall distance between two iris images is computed as the arithmetic mean of the normalized Hamming distance and the cosine dissimilarity computed on the color histogram.

5. Parameters set-up

The segmentation process implemented by WIRE involves several parameters, some of which are strictly related to the size of the object to be segmented from the background. The tuning of all parameters has been performed by evaluating the segmentation/recognition results obtained on a training set, when changing their values. The training set included 50 images randomly picked and not used for testing. The default values of the parameters are those producing the best results in the average during the tuning process.

The most relevant parameters and their assigned values are the following:

- $n=128$ and $\sigma=10$ – kernel size and variance of the Gaussian filter respectively (Section 3.1);
- $\delta=50$ – threshold on color for merging adjacent watershed regions (Section 3.2);
- $th_{curve}=0.5$ – threshold on punctual curvature (Section 3.4);
- $th_{pnt}=150$ – threshold on connected component size for limbus detection (Section 3.4);
- $th_{pupil}=50$ – threshold on connected component size for pupil detection (Section 3.6); and
- $u=3$ and $v=10$ – dimensions for the CSUM cells (Section 4).

As regards size and variance of the Gaussian filter, we noted that there is a quadratic relation between them and the image resolution. The optimal values $n=128$ and $\sigma=10$ have been computed with respect to image resolution in datasets UBIRISv1s2 and UBIRISv2t. For the parameter δ the value 50 has been found as the highest one preventing merging of adjacent watershed regions

belonging to iris and eyelashes that, especially for dark eyes, may be characterized by rather similar colors. In Section 3.4 the threshold th_{curve} is adopted to break the whole foreground contour into separate components depending on punctual curvature. Curvature values range between 0 and 1, and we experimented that points with a curvature higher than the middle value of this range can be deleted from the foreground contour. The parameter th_{pnt} is related to the size of connected component that undergoes to the circle fitting process during limbus detection. We noticed that connected components with less than 150 pixels are too small to be considered as potential candidate for approximating the limbus. Similarly, for the pupil approximation small connected components are discarded in the circle fitting process. As the pupil size is about one third of that of the region delimited by the limbus, we found that 50 represents a good value for this threshold. The performance of the CSUM method strongly depends on size of the cells. We chose the values for these parameters by taking into account the resolution of the iris region in polar space.

6. Experiments and discussion

The used iris images are acquired in visible wavelength. For this reason, WIRE has been tested on the databases UBIRIS version 1 and UBIRIS version 2. Both include color RGB iris images captured on-the-move and at-a-distance, and where images in the latter database are more degraded than those in the former one. UBIRIS version 1 is composed of two sessions, but in order to get the testing process more stressing, only session 2 has been used. Indeed, images acquired in UBIRIS version 1 session 2 (UBIRISv1s2) are more noisy than those collected in session 1, due to specular reflection, defocus, and occlusions. UBIRISv1s2 is composed of 663 images acquired from 132 people (at least 5 images per subject).

Also for UBIRIS version 2, we considered only a subset, named UBIRISv2t. This dataset consists of 1000 images of 171 irises, either left or right. Iris images in UBIRISv2t were selected as training set for the international challenge NICE II. The list of images has been made available at [40]. The subset UBIRISv2t also includes binary iris segmentation masks provided by the algorithm Tan [24] that is the winner of NICE I. The corresponding masks can be considered as the benchmark to compare the effectiveness of WIRE with respect to two additional algorithms, namely ISIS [19] and Wildes [2]. In turn, to compare the performances of selected algorithms on UBIRISv1s2, the binary masks (ground truth) for the iris images have been manually built and should be accepted as the optimal segmentation.

We have used two ground truths for the two datasets for the following reason. The executable version of the algorithm by Tan is not publicly available and we could not run the Tan algorithm on UBIRISv1s2 and, accordingly, used manually segmented masks. In turn, for the dataset UBIRISv2t, we had the results of the Tan algorithm that were made available within the challenge NICE II. Thus, for this dataset we could use the results of the Tan algorithm (used as ground truth) to compare the results of the other algorithms.

To measure the quality of segmentation, two quantitative parameters have been used: (i) the amount of overlap between the segmentation result (i.e. detected binary mask) and the corresponding ground truth; and (ii) the errors percentage measured in pixel number.

Given two binary masks BM_1 and BM_2 , the degree of overlap between them is computed according to the following expression:

$$s_o = \frac{2 \sum_{i,j} BM_1(i,j) \cdot BM_2(i,j)}{\sum_{i,j} BM_1(i,j) + \sum_{i,j} BM_2(i,j)} \quad (8)$$

The value of s_o ranges from 0, when the masks are completely separated, to 1 when they totally overlap. It is worth to notice that the degree of overlap between two binary masks only provides an overall assessment of the segmentation error. In particular, there are cases in which the pupil is not correctly located. Since iris has a larger surface than the pupil, even with an incorrect location of the latter, the amount of overlap still remains high.

To the aim of better evaluating the segmentation accuracy, limbus and pupil location processes must be assessed also separately. Limbus and pupil boundaries produced by the process described in Section 3, are fitted again by circles with Taubin's algorithm. Each circle is described by three parameters that are the planar coordinates of the centre and the radius. The localization errors for the circles approximating limbus and pupil are then computed as the discrepancy in terms of pixel percentage between the parameters of the circles computed by WIRE and those provided by the ground truth.

In more details, for each image in the testing dataset, the absolute value of the difference is computed between homologous parameters (i.e., abscissa, ordinate and radius) of the circle (pupil or limbus) in the ground truth and the corresponding one detected by the tested segmentation approach. The obtained values are normalized according to horizontal/vertical image resolution and are multiplied by 100. The overall is then obtained by averaging errors of all images in the testing dataset.

It has been found experimentally that errors larger than a given threshold ϵ_{out} in circle parameters estimation indicate a completely wrong detection, so that they can be considered as outliers. For each circle parameter, the median value m_d is computed over all errors performed on the testing dataset, and the corresponding ϵ_{out} is set to $15 \cdot m_d$.

Since outliers produce negative effects on the overall evaluation, for each performance a couple of values is showed, specifying if outliers have been included or not in the global average computation. These two cases are always distinguished in the following tables that reassume the results, and for each of them the percentage of outliers is given. Indeed, the percentage of outliers can be used as an additional effectiveness parameter. Finally, to measure how the variations of color and illumination affect the segmentation, each experiment has been repeated with and without the correction step and results are reported in separate tables. Results of this experiment on UBIRISv1s2 images without and with color/illumination correction are reported in Tables 1 and 2, respectively. For each method the results in presence of outliers (out) and without outliers (nout) are reported. The percentage of outliers produced by each method is specified under the corresponding name. Columns 2–4 and 5–7 refer to center coordinates and radius of iris and pupil, respectively, while the last column reports the degree of overlap according expression (8). In each column the smallest error value is highlighted both in

Table 1

Segmentation accuracy measured in terms of error percentage with respect to manual segmentation for the three tested approaches (Wildes, ISIS, and WIRE) on UBIRISv1s2 images without color/illumination correction.

Method		Iris Cx	Iris Cy	Iris radius	Pupil Cx	Pupil Cy	Pupil radius	Overlap
Wildes	out	5.12	1.88	1.44	2.38	7.65	1.55	0.80
	nout	4.52	1.47	1.28	1.63	2.56	1.23	0.83
	11%							
ISIS	out	3.14	3.12	3.15	1.18	1.95	0.93	0.83
	out 4%	3.02	2.84	2.98	0.77	0.91	0.56	0.84
WIRE	out	3.46	2.83	1.03	2.03	2.18	0.97	0.86
	out 6%	2.59	2.32	1.98	1.15	0.98	0.54	0.89

Table 2

Segmentation accuracy measured in terms of error percentage with respect to manual segmentation for the three tested approaches (Wildes, ISIS, and WIRE) on UBIRISv1s2 images with color/illumination correction.

Method		Iris Cx	Iris Cy	Iris radius	Pupil Cx	Pupil Cy	Pupil radius	Overlap
Wildes	out	5.12	1.18	1.44	2.22	7.17	1.47	0.81
	out 9%	4.59	1.48	1.28	1.58	2.49	1.16	0.83
ISIS	out	3.79	3.29	3.15	1.88	2.72	1.15	0.76
	out 12%	2.94	2.59	2.65	1.12	1.19	0.62	0.85
WIRE	out	3.05	2.76	1.91	1.87	2.17	0.93	0.87
	out 4%	2.39	2.09	1.62	1.05	0.94	0.54	0.90

Table 3

Segmentation accuracy measured in terms of error percentage with respect to manual segmentation for the three tested approaches (Wildes, ISIS, and WIRE) on UBIRISv2t images without color/illumination correction.

Method		Iris Cx	Iris Cy	Iris radius	Pupil Cx	Pupil Cy	Pupil radius	Overlap
Wildes	out	6.96	3.78	3.43	8.52	19.55	2.23	0.59
	out 10%	4.54	2.76	3.13	5.92	17.83	1.70	0.65
ISIS	out	2.83	3.30	3.49	2.77	2.23	1.54	0.67
	out 8%	2.40	3.07	3.02	2.08	1.69	1.07	0.72
WIRE	out	4.44	3.95	2.91	4.51	3.34	1.62	0.72
	out 8%	2.87	2.94	2.53	2.58	2.04	1.13	0.78

presence of outliers (number in boldface) and without outliers (numbers in italics).

From Table 1, we can observe that the numbers of outliers provided by ISIS and WIRE are comparable and are both remarkably smaller than that produced by WILDES.

If the outliers are included in the calculation of the average error, the number of parameters for which the error committed by ISIS results to be minimum (in bold) is greater than other two methods.

When the outliers are not included in the calculation of the average error, it appears evident that WIRE almost always performs the best result, as illustrated with the numbers in italics. We remark that with and without outliers WIRE outperforms the other methods in terms of overlap.

On corrected images, the behavior of WIRE radically changes. Indeed, Table 2 shows how WIRE provides the best result with and without outliers in the majority of cases. By comparing results in Tables 1 and 2 we can also observe that the correction process further reduces the number of outliers for two of the tested methods (WILDES and WIRE). This is not true for ISIS, which is deeply based on the Canny filter for pupil localization. However, the Canny filter is rather sensitive to image details, which are greatly accentuated by the correction operator we apply.

The same experiment has been performed on images from the UBIRISv2t dataset without and with color/illumination correction. Results are reported in Tables 3 and 4.

In the first case, that is when no image correction is applied on input images, ISIS shows a higher robustness in terms of centers and radii of iris and pupil, even when the outliers are included. WIRE always outperforms in terms of overlap. Moreover, WIRE comes up as the best performing algorithm on corrected images. Indeed, it is the only method for which the percentage of outliers further reduces. It is also worth noticing that the error percentage generally reduces for all methods when color/illumination correction is applied.

6.1. Impact on iris recognition

Iris location is upstream of the verification/recognition process, so more accurate the segmentation is, higher is the accuracy the overall authentication system will provide. This suggests that the performance of an iris segmentation approach can be indirectly assessed by measuring the improvement in recognition accuracy it induces when placed before a given classification technique. In our case, we compare the recognition performance when the segmented images are those provided by the ground truth and by WILDES, ISIS and WIRE.

The authentication method adopted by WIRE in the experiments is a color extension of the CSUM technique [36] that has been detailed in Section 4. We also try to ascertain the improvement produced by the color/illumination correction in terms of authentication accuracy by testing three abovementioned segmentation approaches (Wildes, ISIS and WIRE) on both UBIRISv1s2 and UBIRISv2t with and without color/illumination correction. According to the protocol defined in NICE II [7], the accuracy of the authentication system has been evaluated in terms of decidability [3]. The decidability measures the performance of an authentication system by evaluating the average of scores it provides for genuine and impostor users. More specifically, given a set of user templates V , it performs an "all-against-all" comparison, which provides a set of dissimilarity intra-class $D_I = \{D_{I1}, D_{I2}, \dots, D_{Ik}\}$ and inter-class $D_E = \{D_{E1}, D_{E2}, \dots, D_{Em}\}$, depending on whether templates belong to the same class or not. The decidability $d(D_I, D_E)$ of the set V is computed as follows:

$$d(D_I, D_E) = \frac{|avg(D_I) - avg(D_E)|}{\sqrt{\frac{1}{2} (\sigma(D_I)^2 + \sigma(D_E)^2)}} \quad (9)$$

where the resulting value ranges into $[0, \infty)$.

Tests have been performed on both UBIRISv1s2 and UBIRISv2t, and results are reported in Tables 5 and 6, respectively. Tables 5 and 6 regard the performance of iris recognition for UBIRISv1s2 and UBIRISv2t respectively. In both cases, the first column provides the recognition performance (decidability) obtained when the ground truth is used as the result of segmentation.

Table 4

Segmentation accuracy measured in terms of error percentage of error with respect to manual segmentation for the three tested approaches (Wildes, ISIS, and WIRE) on UBIRISv2t images with color/illumination correction.

Method		Iris Cx	Iris Cy	Iris radius	Pupil Cx	Pupil Cy	Pupil radius	Overlap
Wildes	out	5.79	3.57	3.52	6.53	9.48	1.83	0.63
	out 16%	4.25	2.69	3.17	4.93	3.56	1.50	0.67
ISIS	out	3.87	3.39	2.76	4.12	3.10	1.54	0.68
	out 8%	2.45	2.63	2.49	2.43	2.02	1.19	0.74
WIRE	out	3.35	2.87	2.57	3.55	2.58	1.46	0.77
	out 6%	2.41	2.31	2.33	2.17	1.53	1.02	0.81

Table 5

The decidability for recognition on UBIRISv1s2 images, when segmentation mask are those provided by the ground truth, Wildes, ISIS and WIRE.

Dataset	Ground truth	Wildes	ISIS	WIRE
UBIRISv1s2 no correction	2.1476	2.0335	1.3801	2.0356
UBIRISv1s2 with correction	2.1455	2.0324	1.3800	2.0335

Table 6

The decidability for recognition on UBIRISv2t images, when segmentation mask are those provided by the ground truth, Wildes, ISIS and WIRE.

Dataset	Ground truth	Wildes	ISIS	WIRE
UBIRISv2t no correction	1.2472	1.0211	0.6469	1.3755
UBIRISv2t with correction	1.3926	0.8062	1.0985	1.3850

As expected, Table 5 confirms that manual segmentation (ground truth) is the most accurate, since it allows the classifier to reach the highest value of decidability. Moreover, there is no appreciable difference between decidability values obtained with and without color/illumination correction. This is motivated by the fact that changes in lighting and color temperature are quite limited on the images of the UBIRISv1s2 dataset.

Several interesting aspects come up from values reported in Table 6. First of all, the decidability induced by WIRE on the original images (no correction) is higher than that produced by all other approaches; moreover, it still remains comparable after color/illumination correction underlying in this way the robustness of WIRE with respect to local distortions. The correction process also produces a considerable increase in decidability values when using the ground truth and ISIS segmented images. On the contrary, the method suggested by Wildes suffers from a high location error for pupil parameters, which strongly affects the classification process and leads to a reduction of the decidability value.

7. Conclusion

The growing interest of the research community for iris based identification under uncontrolled data acquisition conditions inspired this paper. Moreover, the future capillary diffusion of HD camera will make iris detection more and more strategic in the identification process. So a novel watershed based iris segmentation scheme, namely WIRE, has been designed and tested for visible wavelength noisy images. The experimental results, performed on UBIRIS version 1 session 2 and the subset of UBIRIS version 2 used as training set for the international challenge NICE II, demonstrated the robustness of WIRE in terms of accuracy. This is relevant to security and surveillance, on one side, and mobile commercial and financial applications (home and mobile banking), on the other side. To further improve performances we plan to use a suitable binarization of the watershed transform also for pupil detection, so as to increase the accuracy in the location of pupil boundary. We are also planning to exploit watershed based iris detection for NIR eye images and to extend WIRE to mobile framework.

References

- [1] J. Daugman, The importance of being random: statistical principles of iris recognition, *Pattern Recognit.* 36 (2) (2003) 279–291.
- [2] R. Wildes, Iris recognition: an emerging biometric technology, *Proc. IEEE* 85 (9) (1997) 1348–1363.
- [3] J.G. Daugman, How iris recognition works, *IEEE Trans. Circuits Syst. Video Technol.* 1 (14) (2004) 21–30.
- [4] N.B. Puhan, N. Sudha, A novel iris database indexing method using the iris color, In: *Proceedings of the IEEE Conference on Industrial Electronics and Applications*, 2008, pp. 1886–1891.
- [5] Special issue on: Segmentation of visible wavelength iris images captured at-a-distance and on-the-move, *Image Vis. Comput.* 28 (2) (2010) 213–284.
- [6] Special issue on: noisy iris challenge evaluation II – recognition of visible wavelength iris images captured at-a-distance and on-the-move, *Pattern Recognit. Lett.* 33 (8) (2012) 963–1026.
- [7] H. Proença, L. Alexandre, Toward covert iris biometric recognition: experimental results from the NICE contests, *IEEE Trans. Inf. Forensics Secur.* 2 (7) (2012) 798–808.
- [8] J.C. Daugman, High confidence visual recognition of persons by a test of statistical independence, *IEEE Trans. Pattern Anal. Mach. Intell.* 11 (15) (1993) 1148–1161.
- [9] M. Burge, K.W. Bowyer, *Handbook of Iris Recognition*, Springer, London, UK, 2013.
- [10] K.W. Bowyer, K.P. Hollingsworth, P.J. Flynn, Image understanding for iris biometrics: a survey, *Comput. Vis. Image Underst.* 110 (2) (2008) 281–307.
- [11] K.W. Bowyer, K.P. Hollingsworth, P.J. Flynn, A survey of iris biometrics research: 2008–2010, in: M. Burge, K.W. Bowyer (Eds.), *Springer*, 2013, pp. 15–54 (Chapter 2).
- [12] J. Daugman, C. Downing, No change over time is shown in Rankin et al., “Iris recognition failure over time: the effects of texture”, *Pattern Recognit.* 46 (2) (2013) 609–610.
- [13] D.M. Rankin, B.W. Scotney, P.J. Morrow, B.K. Pierscionek, Iris recognition failure over time: the effects of texture, *Pattern Recognit.* 45 (1) (2012) 145–150.
- [14] D.M. Rankin, B.W. Scotney, P.J. Morrow, B.K. Pierscionek, Iris recognition—the need to recognise the iris as a dynamic biological system: response to Daugman and Downing, *Pattern Recognit.* 46 (2) (2013) 611–612.
- [15] H. Proença, L.A. Alexandre, UBIRIS: a noisy iris image database, In: *Proceedings of the International Conference on Image Analysis and Processing*, 2005, pp. 970–977.
- [16] H. Proença, S. Filipe, R. Santos, J. Oliveira, L.A. Alexandre, The UBIRIS.v2: a database of visible wavelength iris images captured on-the-move and at-a-distance, *IEEE Trans. Pattern Anal. Mach. Intell.* 32 (8) (2010) 1529–1535.
- [17] J. Illingworth, J. Kittler, A survey of the Hough transform, *Comput. Vis. Graph., Image Process.* 1 (44) (1988) 87–116.
- [18] S.A. Sahnoud, I.S. Abuhaija, Efficient iris segmentation method in unconstrained environments, *Pattern Recognit.* 46 (12) (2013) 3174–3185.
- [19] M. De Marsico, M. Nappi, D. Riccio, IS_1S: iris segmentation for identification systems, In: *Proceedings of the International Conference on Pattern Recognition (ICPR 2010)*, 2010, pp. 2857–2860.
- [20] G. Taubin, Estimation of planar curves, surfaces and nonplanar space curves defined by implicit equations, with applications to edge and range image segmentation, *IEEE Trans. Pattern Anal. Mach. Intell.* 13 (13) (1991) 1115–1138.
- [21] Z. He, T. Tan, Z. Sun, X. Qiu, Toward accurate and fast iris segmentation for iris biometrics, *IEEE Trans. Pattern Anal. Mach. Intell.* 9 (31) (2009) 1670–1684.
- [22] D.S. Jeong, J.W. Hwang, B.J. Kang, K.R. Park, C.S. Won, D.-K. Park, J. Kim, A new iris segmentation method for non-ideal iris images, *Image Vis. Comput.* 28 (2) (2010) 254–260.
- [23] H. Proença, Iris recognition: on the segmentation of degraded images acquired in the visible wavelength, *IEEE Trans. Pattern Anal. Mach. Intell.* 8 (32) (2010) 1502–1516.
- [24] T. Tan, Z. He, Z. Sun, Efficient and robust segmentation of noisy iris images for non-cooperative iris recognition, *Image Vis. Comput.* 2 (28) (2010) 223–230.
- [25] A. Ross, S. Shah, Segmenting non-ideal irises using geodesic active contours, In: *Proceedings of Biometrics Symposium (BSYM)*, 2006, pp. 824–836.
- [26] S. Shah, A. Ross, Iris segmentation using geodesic active contours k, *IEEE Trans. Inf. Forensics Secur.* 4 (4) (2009) 824–836.
- [27] K. Roy, P. Bhattacharya, Variational level set method and game theory applied for nonideal iris recognition, In: *Proceedings of the International Conference on Image Processing (ICIP)*, 2009, pp. 2721–2724.
- [28] K. Roy, P. Bhattacharya, C.Y. Suen, Iris segmentation using variational level set method, *Opt. Lasers Eng.* 49 (4) (2011) 578–588.
- [29] M. Vatsa, R. Singh, Improving iris recognition performance using segmentation, quality enhancement, match score fusion, and indexing, *IEEE Trans. Syst. Man Cybern. Part B: Cybern.* 38 (4) (2008) 1021–1035.
- [30] X. Zhang, S.Z. Sun, T. Tan, Texture removal for adaptive level set based iris segmentation, In: *Proceedings of the International Conference on Image Processing (ICIP 2010)*, 2010, pp. 1729–1732.
- [31] S. Beucher, C. Lantuejoul, Use of watersheds in contour detection, In: *Proceedings of the International Workshop on Image Processing, Real-Time Edge and Motion Detection/Estimation*, France, 1979.
- [32] M. Marcon, E. Frigerio, S. Tubaro, Sclera segmentation for gaze estimation and iris localization in unconstrained images, in: P. Di Giambardino, D. Iacoviello, J.M.R.S. Tavares, R.M. Natal Jorge (Eds.), *CRC Press*, 2012, pp. 25–30.
- [33] M. Frucci, M. Nappi, D. Riccio, G. Sanniti di Baja, Using the watershed transform for iris detection, In: *Proceedings of the International Conference on Image Analysis and Processing (ICIAP 2013)*, 2013, pp. 269–278.
- [34] M. Frucci, M. Nappi, D. Riccio, Watershed based iris segmentation, In: *Proceedings of the 5th Mexican Conference on Pattern Recognition (MCPR 2013)*, 2013, pp. 204–212.
- [35] A.F. Mat Raffei, H. Asmuni, R. Hassan, R.M. Othman, Feature extraction for different distances of visible reflection iris using multiscale sparse representation of local Radon transform, *Pattern Recognit.* 46 (10) (2013) 2622–2633.
- [36] E. Raj, M. Chirchi, R.D. Kharadkar, Biometric iris recognition for person identification using cumulative sum algorithm, *Int. J. Sci. Eng. Res.* 3 (5) (2012).

[37] B.K.P. Horn, *Robot Vision*, MIT Press, Cambridge, MA, 1997.

[38] M. De Marsico, M. Nappi, D. Riccio, G. Tortora, NABS: novel approaches for biometric systems, *IEEE Trans. Syst. Man Cybern. Part C* 41 (4) (2011) 481–493.

[39] J.B.T.M. Roerdink, A. Meijster, The watershed transform: definitions, algorithms and parallelization strategies, *Fundam. Inform.* 41 (1–2) (2001) 187–228.

[40] (http://www.bioplab.unisa.it/UBIRISv2t_image_list.txt), last visited on 11/03/2013.

Maria Frucci is a senior researcher. She received the laurea degree (cum laude) in Physics from the “Federico II University” of Naples, Italy, in 1983. In the period 1984–1987 she worked at the Centre for Informatics and Industrial Automation Research, Portici, Italy, where she was active in the area of Natural Language, Expert Systems and Shape Analysis. She moved to the Institute of Cybernetics E. Caianiello of the National Research Council of Italy (CNR), in 1988 and to the Institute for High-Performance Computing and Networking, CNR, Naples in 2014. She had a teaching contract with the University “Federico II” of Naples, Italy. She is member of the International Association for Pattern Recognition. From 2008 to 2012, she has been a member of the Governing Board of the Italian Group of Italian Researcher in Pattern Recognition (GIRPR). Her research activity is mainly in the field of image processing and pattern recognition. Her main interests include shape representation and analysis, biometrics, description and segmentation.

Michele Nappi was born in Naples, Italy, in 1965. He received the Laurea degree (cum laude) in computer science from the University of Salerno, Salerno, Italy, in 1991, the M. Sc. degree in information and communication technology from the International Institute for Advanced Scientific Studies “E.R. Caianiello,” Vietri sul Mare, Salerno, and the Ph.D. degree in applied mathematics and computer science from the University of Padova, Padova, Italy. He is currently an Associate Professor of computer science at the Università di Salerno. His research interests include pattern recognition, image processing, compression and indexing, multimedia databases, and visual languages. Dr. Nappi is a member of the International Association for Pattern Recognition.

Daniel Riccio was born in Cambridge, U.K., in 1978. He received the Laurea degree (cum laude) and the Ph.D. degree in computer science from the University of Salerno, Salerno, Italy, in 2002 and 2006, respectively. He is currently an Associate Professor at the University of Naples, Federico II. His research interests include biometrics, fractal image compression, and indexing. Dr. Riccio is a IEEE member since 2012. He is also a member of the Italian Group of Italian Researcher in Pattern Recognition since 2004.

Gabriella Sanniti di Baja was born in 1950, received the laurea degree (cum laude) in physics from the “Federico II University” of Naples, Italy, in 1973, and the Ph.D. honoris causa from the Uppsala University, Sweden, in 2002. Since 1973, she has been working in the field of image processing and pattern recognition at the Institute of Cybernetics E. Caianiello of the Italian National Research Council (CNR), where she has been the director of research until she retired in February 2015. She is currently an Associate Researcher at the Institute for High Performance Computing and Networking, CNR. Her research interests include 2D and 3D shape representation and analysis. She has published a number of papers in international journals and conference proceedings, is the coeditor-in-chief of *Pattern Recognition Letters*, has been President of the International Association for Pattern Recognition (IAPR) as well as of the Italian Group of Researchers in Pattern Recognition (GIRPR), is IAPR Fellow and Foreign Member of the Royal Society of Sciences at Uppsala, Sweden.